Journal of Materials Chemistry A

RSC Publishing

PAPER

View Article Online
View Journal | View Issue

Synthesis of Mg_2Cu nanoparticles on carbon supports with enhanced hydrogen sorption kinetics†

Cite this: *J. Mater. Chem. A*, 2013, **1**, 9983

Yuen S. Au,[a] Marine Ponthieu,[b] Rien van Zwienen,[a] Claudia Zlotea,[b] Fermin Cuevas,[b] Krijn P. de Jong[a] and Petra E. de Jongh*[a]

Received 5th March 2013
Accepted 16th June 2013

DOI: 10.1039/c3ta10926g

www.rsc.org/MaterialsA

The reaction kinetics and reversibility for hydrogen sorption were investigated for supported Mg_2Cu nanoparticles on carbon. A new preparation method is proposed to synthesize the supported alloy nanoparticles. The motivation of using a support is to separate the nanoparticles to prevent sintering at elevated temperatures. Supported nanocrystallites with an average size of 20 nm were obtained on porous graphite and larger particles (~300 nm) on non-porous graphite by first deposition of metallic Cu species, using solution impregnation, followed by addition of molten Mg and hydrogenation. The temperature for hydrogen release of the 20 nm particles was much lower (~150 °C) than the micron-sized material, and the reaction was reversible with the same improved kinetic performance after several hydrogen sorption cycles. The 20 nm Mg_2Cu crystallites had a lower activation energy for the hydrogen desorption reaction compared to the bulk material (97 (±9) and 128 (±6) kJ mol^{-1} respectively). A desorption enthalpy of 66 (±3) kJ mol^{-1} and an entropy value of 126 (±10) J $mol\ K^{-1}$ were found for this system. The use of a porous carbon support was beneficial for obtaining Mg_2Cu nanoparticles, which improved the hydrogen sorption kinetics.

Introduction

The decrease in our fossil fuel reserves has led to an increasing interest in producing energy from renewable sources. Hydrogen is a promising candidate to act as a sustainable energy carrier in the future. But to allow usage of hydrogen as an energy carrier, an efficient and safe way for storage is required. Hydrogen storage in a solid could be a solution.

Magnesium is a promising material for hydrogen storage and has been widely studied because of its light weight and natural abundance. It can store hydrogen directly, forming MgH_2, which contains 7.7 wt% of hydrogen. However, it suffers from slow hydrogen sorption kinetics and has a high thermodynamic stability, since the equilibrium temperature for the hydrogen sorption reaction is around 300 °C for 1 bar of H_2 pressure. Many investigations have been conducted on Mg as a potential hydrogen storage material to improve the reaction kinetics and to change the thermodynamic stability in order to shift the reaction equilibrium to ambient conditions.[1,2]

One way to improve the kinetics of the hydrogen sorption reaction is to add a catalyst. Doping small amounts of other metals such as Ti, V, Mn, Fe and Ni has led to enhanced hydrogen sorption kinetics and lowered the activation energy for hydrogen desorption of MgH_2.[3] Also, the addition of small amounts of metal oxides like Nb_2O_5 resulted in improved kinetic performance.[4] Another method to alter the hydrogen storage properties of Mg is to form intermetallics. For example, Mg–Ni or Mg–Al forms stable intermetallics.[5,6] Some of these intermetallic compositions can form ternary hydrides upon hydrogenation like the well known Mg_2NiH_4. Moser *et al.* were able to synthesize ternary hydrides with Ti, Zr, Hf, V, Nb and Ta.[7] The enthalpy of formation for these ternary hydrides is usually less negative than pure MgH_2, so that hydrogen can be released at lower temperatures for these systems.

Another way to improve hydrogen sorption properties is by nanosizing the material. In general, reducing the particle or crystallite size improves the access for H_2 to enter the lattice by the increased surface area to volume ratio. Also, the diffusion distance for hydrogen molecules through the crystal lattice is decreased. Mechanical alloying, arc-discharge and colloid synthesis have been used to prepare nanostructured Mg based intermetallics and altered kinetic behavior for hydrogen sorption was reported.[8–14] An important issue is sintering of the nanostructures at high temperatures, which will diminish the benefits obtained.[15] The formation of large particles is energetically favorable due to their lower specific surface area compared to small particles. A microscopy study by Beattie *et al.* has shown that small Mg particles formed an agglomerated network after heating to 400 °C.[16]

[a]*Inorganic Chemistry and Catalysis, Debye Institute for Nanomaterials Science, Utrecht University, Universiteitsweg 99, 3584 CG Utrecht, The Netherlands. E-mail: p.e.dejongh@uu.nl*

[b]*ICMPE/CNRS-UPEC UMR 7182, 2-8 rue Henri Dunant, 94320 Thiais, France*

† Electronic supplementary information (ESI) available: XRD patterns of Cu and Mg_2Cu synthesized on non-porous carbon (KS-6). Kissinger plots of $Mg_2Cu(H)$ on porous carbon, non-porous carbon and bulk. See DOI: 10.1039/c3ta10926g

To prevent sintering, one can disperse the metal particles over a support material. The support material should be inert to prevent a reaction between the support and the deposited metal species. Most hydrogen storage materials are susceptible to oxidation and form stable oxides, which is an irreversible reaction. Mg is no exception, thus any material containing oxygen species is not suitable. This narrows the choice down to carbon support materials. Carbon is inert towards most metal compositions and depending on the morphology of the carbon material, particle sizes can be controlled during the synthesis process. Quite a number of hydrogen storage systems supported or embedded in carbon have already been studied.[17–19] Earlier work in our group showed that we were able to synthesize nanosized Mg–Ni composites by using a carbon support.[20] We obtained a mixture of nanostructured Mg_2NiH_4 and Ni catalyzed nano-MgH_2 particles and improved hydrogen desorption properties were observed.

The aim of the work described was to modify the hydrogen sorption properties of MgH_2 by investigating the possibility of synthesizing supported Mg_2Cu nanoparticles on carbon. Next to the challenge of obtaining a pure phase of supported alloy nanoparticles, this model system could also demonstrate the synergetic effect of supported nanoparticles and the addition of a transition metal to change the thermodynamic equilibrium. So far, no ternary hydride of the Mg–Cu system has been reported in the literature. The role of Cu is to substitute H_2 in MgH_2 to form the stable Mg_2Cu compound, leading to a lower desorption enthalpy compared to pure MgH_2. Reilly and Wiswall[21] were one of the first to investigate the hydrogen sorption properties of the bulk Mg_2Cu intermetallic system. They found that this system can reversibly store up to 2.6 wt% of hydrogen following the reaction:

$$2Mg_2Cu + 3H_2 \leftrightarrow 3MgH_2 + MgCu_2 \quad (1)$$

They also reported that the enthalpy for the hydrogen desorption reaction is approximately 5.9 kJ mol^{-1} lower compared to the pure MgH_2 system. Next to diffusion of hydrogen through the material as in pure MgH_2, this reaction also requires solid state diffusion of Mg to go from the Mg-poor to the Mg-rich state of the alloy and *vice versa*. Solid-state diffusion is slow and requires thermal activation. Nanosizing this intermetallic system could improve the reaction kinetics by shortening the diffusion distance of the Mg atoms to perform reaction (1).

Bulk Mg_2Cu can be crystallized from a melt with the correct stoichiometric Mg : Cu ratio as indicated by the phase diagram of the Mg–Cu system in Fig. 1.[22] However, it is not trivial to prepare nanoparticles from a melt due to the high vapor pressure of Mg and possible demixing of the alloy phase. Our alternative synthesis strategy is to use a support material to obtain small and well dispersed alloy particles. In this way the particles are prevented from sintering at elevated temperatures. A method to deposit small metallic Cu particles on a support material is to use solution impregnation techniques, which are widely applied in catalyst preparation.[23,24]

The addition of Mg is not as straightforward as Cu. Mg easily reacts irreversibly with other species, such as oxygen, to form

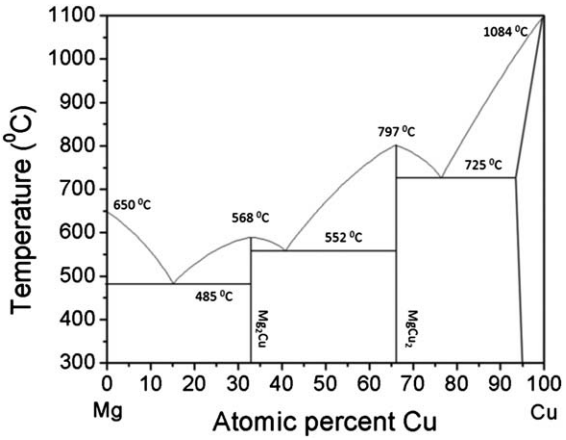

Fig. 1 Phase diagram of the Mg–Cu system.

stable compounds, thereby greatly limiting the choice for suitable precursors to perform a second impregnation or co-impregnation with a suitable solvent. On the other hand, we have developed a method to disperse Mg nanoparticles over carbon with a melting process.[25] Therefore, we synthesized Mg_2Cu in two steps by first depositing small Cu particles on the support followed by a melting process, where molten Mg reacts with the supported Cu particles. We will show the characteristics of the obtained intermetallic compositions on two different carbon supports. Different particle sizes were obtained and they showed different kinetic behavior for hydrogen desorption.

Experimental

Sample preparation

The first step in preparing Mg_2Cu on carbon was to perform incipient-wetness impregnation to deposit small Cu particles on the carbon support. An aqueous solution of 2.5 M $Cu(NO_3)_2 \cdot 3H_2O$ (Sigma-Aldrich) was used. The solution was acidified to a pH of 1 with nitric acid to prevent the precipitation of basic nitrates during the impregnation procedure. Two different carbon supports were used. One was a porous carbon material (Timcal High Surface Area Graphite (HSAG)) with a surface area of 500 $m^2\ g^{-1}$ and with a total pore volume of 0.66 $cm^3\ g^{-1}$. The other was a non-porous graphite material (Timcal KS-6) with a surface area of 21 $m^2\ g^{-1}$. The carbons were degassed at 600 °C overnight in an Ar atmosphere to remove all traces of moisture.

The dry carbons (1 g) were impregnated with 0.66 ml of the $Cu(NO_3)_2$ solution under an Ar atmosphere, followed by drying in vacuum at room temperature overnight. For decomposition of the precursor and reduction to obtain metallic Cu particles, the sample was heated to 230 °C with a temperature ramp of 1 °C min^{-1} and a dwell time of 30 min under a 20% H_2 in Ar gasflow of 300 ml min^{-1}. All further sample handling for the next synthesis steps was performed in an Ar-glove box (MBraun Labmaster) and excluded from contact with air.

The next step was to perform the melting of Mg with the presence of the Cu–C materials following a procedure as described in the literature.[25] MgH_2 (Alfa Aesar 98%) was used as

a precursor. The Cu–C composite (1.0 g) was mixed with MgH_2 (85 mg) and ground in a mortar. The molar ratio of Mg : Cu was 2.25 : 1, which is slightly higher than the stoichiometric amount of Mg_2Cu. An excess of Mg was used to avoid the formation of $MgCu_2$.[22] The final composites consist of 15 wt% Mg_2Cu on carbon. A reference sample containing 10 wt% MgH_2 on porous carbon (Timcal High Surface Area Graphite) was prepared with the same procedure. Hydrogenation of the samples was performed in high pressure autoclaves (Parr) at 300 °C and H_2 pressures around 80 bars for 12 hours. The hydrogenated samples are designated as $Mg_2Cu(H)$.

Bulk Mg_2Cu was synthesized by induction melting. A Cu-plate (Chempur 99.99%) was wrapped around a Mg-rod (Chempur 99.9%) and placed in a Ta-foil crucible. The exact molar ratio of 2 : 1 was used for Mg and Cu respectively. The sample was placed in a sealed quartz tube and brought into the coil of the induction furnace. The quartz tube with the sample was evacuated and refilled with Ar before the current of the induction furnace was slowly increased until a molten mixture was observed. The molten metal mixture was kept under the same current for 30 min followed by cooling to room temperature. After the reaction was completed, the alloy was heated under Ar in a tubular resistance furnace at 470 °C for 1 day to ensure chemical homogeneity. Lastly, the sample was powdered in a mortar and sieved to obtain particles smaller than 10 microns. This sample was used for reference purposes either in a bare state or physically mixed (15 wt%) with porous carbon.

Structural characterization

The crystalline phases of the samples were analyzed with X-ray diffraction (XRD) (Bruker D8 equipped with VANTEC-1 detector and using Co $K\alpha_{1,2}$ radiation in an airtight sample holder). Data were collected from 20° to 105° 2θ with a step size of 0.1° with an acquisition time of 2 s per step. The data were refined by using the Rietica program.[26]

N_2-physisorption (Micromeritics TriStar 3000) was performed at 77 K for porosity analysis. Barrett–Joyner–Halenda (BJH) analysis on the adsorption isotherms, using a carbon black reference for the thickness equation, provided information on the pore-size distribution of the meso-pores. The total pore volume was obtained at $P/P_0 = 0.997$. Leaching of the Mg–Cu from the nanocomposite was done in a diluted nitric acid solution (pH ~ 2.5) and stirred overnight, followed by filtration and washing with demineralized water until the pH was neutral. This sample was dried under He at 200 °C before measurement. The other samples were prepared in a capped quartz sample tube in the glovebox and were directly measured.

A Scanning Electron Microscope (SEM) (Philips XL30S FEG equipped with embedded energy-dispersive X-ray spectroscopy (EDX) and low kilovolt backscatter detectors) was used to obtain micrographs from back-scattered electrons (BSE). The samples were prepared in air by spreading a thin powder layer on sticky carbon. For Transmission Electron Microscopy (TEM), a part of the sample was stored in air and a small amount of the sample was put on a 200 mesh Ni grid coated with a carbon polymer film. The microscope images were taken with an FEI Tecnai 20F (equipped with a Field Emission Gun) and operated at 200 kV in bright field mode.

Hydrogen sorption measurements

Temperature Programmed Desorption (TPD) (Micromeritics AutoChem II 2920) measurements were performed to obtain kinetic data on hydrogen release. Approximately 100 mg of sample was taken for each measurement. The experiments were carried out in an Ar-flow of 25 ml min^{-1} with a temperature ramp of 5 °C min^{-1} and dwelled at 450 °C for 20 min. To allow Kissinger analysis, the temperature ramps were varied from 1 °C min^{-1}, 2 °C min^{-1}, 5 °C min^{-1} to 10 °C min^{-1}.

Cycling performance of the material was tested gravimetrically after activation with a magnetic suspension balance (Rubotherm). Desorption was measured under 1.3 bars of H_2 with a temperature ramp of 1 °C min^{-1} up to 380 °C and absorption at 300 °C under 50 bars of H_2 for 5 hours. Activation of the material was performed *ex situ* in an autoclave. Absorption occurred at 325 °C and 50 bar H_2 pressure for 10 h and desorption was performed in a vacuum for 2 h at the same temperature.

H_2 desorption isotherms were also measured volumetrically by using Sieverts' method (Setaram PCT PRO-2000). The sample was placed in a steel holder, which was covered with graphite foil (PAPYEX®) on the inside to prevent side reactions at temperatures above 350 °C (ESI, Fig. 1†). The hydrogen desorption measurements were performed at 250 °C, 300 °C, 325 °C and 350 °C with pressure steps of 2 bar H_2. Two boundary conditions were set for obtaining an equilibrium: a minimum kinetic rate of 1×10^{-4} wt% (H_2) min^{-1} and a time limit of 150 min. Rehydrogenation was performed *in situ* at 300 °C and 50 bars of H_2 for 12 hours.

Results and discussion

Structural characterization of the Cu–C composites

The X-ray diffraction patterns show only C and Cu diffraction lines for both the porous (Fig. 2(a)) and non-porous carbon supports (ESI, Fig. 2†) after Cu impregnation and reduction. Profile fitting with Rietveld refinement confirms that only metallic Cu ($Fm\bar{3}m$) on graphitic carbon ($P6_3/mmc$) was present as a crystalline phase. The average crystallite size of Cu on porous carbon was 10 nm, which was calculated from the line width at half maximum of all the Cu diffraction lines. A larger average crystallite size of 30 nm for Cu on non-porous carbon was calculated from its diffraction pattern.

SEM with backscattered electrons shows the difference between the Cu particle sizes obtained on the porous and non-porous supports (Fig. 3(a) and (b)). The obtained Cu particles were much smaller on porous carbon and the distribution of the particles was quite homogeneous over the porous carbon support. This probably prevented the growth of the Cu particles during the reduction step. So, using High Surface Area Graphite was better for obtaining small Cu particles with a uniform distribution.

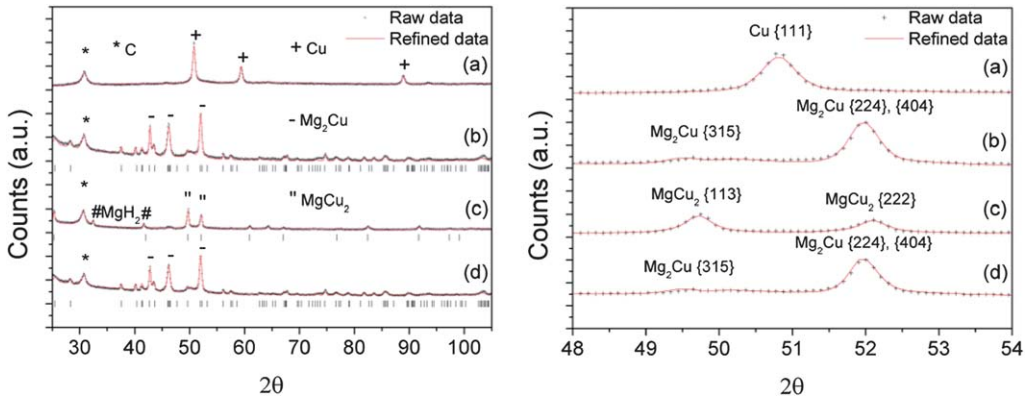

Fig. 2 XRD patterns obtained after Cu impregnation on porous carbon (a), melt infiltration (b), hydrogenation (c) and dehydrogenation (d). A selected region is enlarged for clarity (right frame). The strongest lines belonging to C(*), Cu(+), MgH_2(#), Mg_2Cu (–) and $MgCu_2$('') are indicated. (|) Underneath the patterns represents the position of all the reflections for Mg_2Cu (b and d) and $MgCu_2$ (c).

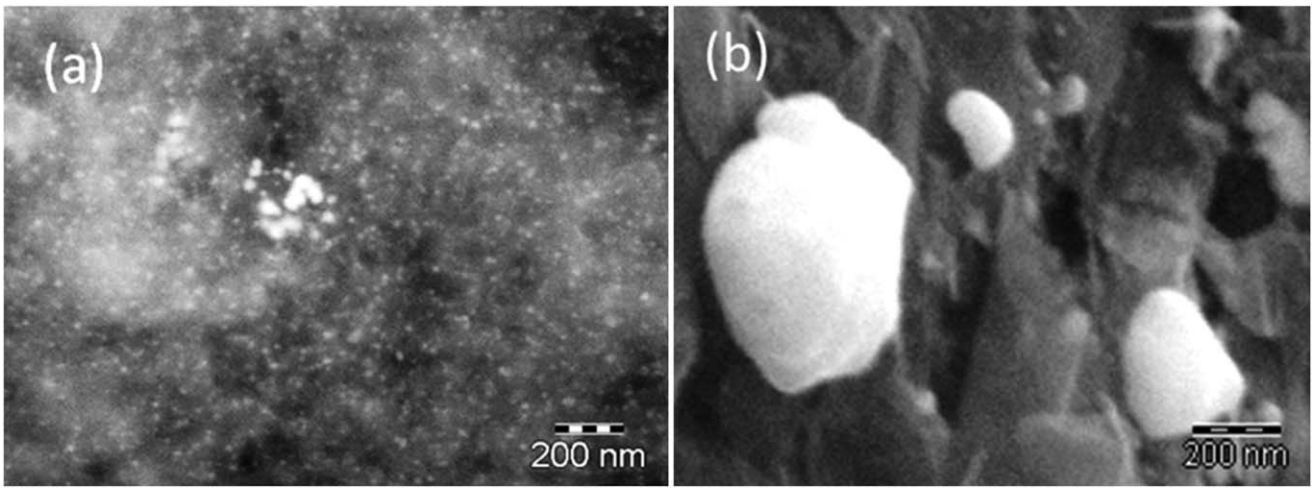

Fig. 3 SEM-images from back-scattered electrons of: (a) Cu on porous carbon and (b) Cu on non-porous carbon.

Fig. 4 shows the obtained N_2-physisorption isotherms and the derived pore size distribution of the porous carbon support. The shape of the nitrogen sorption isotherm (Fig. 4a and b) did not change after the deposition of Cu, so the structure of the pores did not change; however, a gradual decrease of the porosity was observed. The decrease in pore volume is observed mainly in the 2–20 nm region (Table 1). This suggests that some Cu particles might occupy these pores. However, the pore volume loss is larger than expected. To verify whether the pore structure was changed, the metals were leached from the carbon in an acidic solution and the sample was re-measured (Fig. 4(d)). The total pore volume was recovered after this treatment, so no severe damage to the carbon structure has occurred. The extra loss in pore volume might be caused by blockage of the pores by the Cu particles. Clearly, these observations again stress that porous carbon is better for obtaining small Cu particles compared to non-porous carbon, because porous carbon was able to prevent agglomeration of the Cu particles during the drying and reduction step by providing a larger surface area and partial entrapment of the Cu particles inside its pores.

Structural characterization of the Mg_2Cu–C composites

XRD was performed again after the reaction with Mg to analyze new crystalline phases. The diffraction pattern (Fig. 2b) fitted well with the structure models of Mg_2Cu (*Fddd*) and graphitic carbon ($P6_3/mmc$) using Rietveld refinement.[27] Calculation from the line width of the 5 strongest diffraction lines of the Mg_2Cu phase yielded average Mg_2Cu crystallites of 20 nm on the porous carbon material, while much larger Mg_2Cu crystallites were present on non-porous carbon graphite. The excess of Mg successfully prevented the formation of $MgCu_2$, but no additional Mg diffraction lines were observed. The absence of these diffraction lines could be due to evaporation of Mg, which has a high vapor pressure, during the melting reaction. Alternatively, very small Mg particles might have formed within the carbon pores, which could not be detected by XRD.

The electron microscope images of different Mg_2Cu composites are shown in Fig. 5. The TEM image in Fig. 5(a) visualizes Mg_2Cu on porous carbon. The dark spheres represent the Mg_2Cu alloy and carbon is observed as a plate like structure

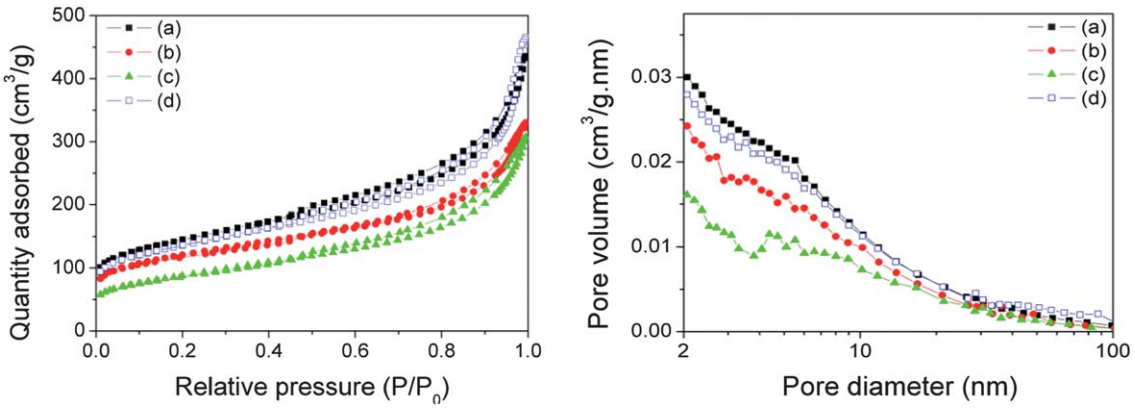

Fig. 4 Nitrogen isotherms (left) and pore size distribution (right) of: (a) HSAG-500, (b) after Cu impregnation, (c) after addition of Mg and (d) after removal of all metal species.

Table 1 Calculated values for the Brunauer–Emmet–Teller (BET) surface area (S_{BET}), meso-pore volume ($V_{2–50\ nm}$), single point total pore volume (V_{total}) and expected total pore volume loss (V_{ex}) of HSAG-500 assuming all metals are inside the pores

Sample	S_{BET} ($m^2\ g^{-1}$)	$V_{2–20\ nm}$ ($cm^3\ g^{-1}$)	V_{total} ($cm^3\ g^{-1}$)	V_{ex} ($cm^3\ g^{-1}$)
(a) HSAG-500	499	0.24	0.66	—
(b) Cu–C	467	0.19	0.56	0.02
(c) Mg_2Cu–C	291	0.14	0.51	0.05
(d) C leached	470	0.23	0.71	—

in grey. The size of the dark spheres varies from 10 nm to 50 nm, but most particles had a size close to 25 nm. Larger Mg_2Cu particles were observed in the SEM-image for the sample prepared on non-porous carbon Fig. 5(b). The image from back-scattered electrons shows the spherical alloy particles in white. The graphite plates are visible in dark grey. The particles varied in size between 100 nm and 500 nm. The majority of the particles was 300 nm in size. The SEM image of the sieved fraction of bulk Mg_2Cu, which was physically mixed with porous carbon, is shown in Fig. 5(c). Most crystals have a size up to a few micrometers. The histogram of the particle size distribution of Mg_2Cu on porous and non-porous carbon is shown in Fig. 5(d). In summary, samples with a different size range were obtained.

N_2-physisorption of Mg_2Cu on porous carbon (Fig. 4c) shows a further decrease in pore volume compared to Cu on porous carbon, which was approximately the expected loss due to addition of Mg (Table 1). BJH analysis of the pore size distribution shows a gradual decrease of the pore volume in the region between 2 and 20 nm and follows the same trend as the previous measurement on the Cu–C composite (Fig. 4b). Therefore, Mg successfully reacted with the small Cu particles to form nano-sized alloy particles. In contrast, large alloy crystals were formed on non-porous carbon due to agglomeration during the reaction. The crystal growth on porous carbon was surprisingly limited.

The XRD pattern in Fig. 2(c) shows the obtained crystalline phases after hydrogenation. New peaks have appeared, which corresponds to crystalline MgH_2 ($P4_2/mnm$) and $MgCu_2$ ($Fd3m$).[28] The peaks around 50° and 52° show the transformation of the Mg_2Cu to the $MgCu_2$ lattice and two new strong diffraction lines around 32° and 42° are from the MgH_2 phase. XRD after dehydrogenation yielded the pattern in Fig. 2(d), which is identical to the pattern obtained after synthesis of the alloy (Fig. 2(b)). Similar results were observed for the samples synthesized on non-porous carbon, where the observed diffraction lines were sharper compared to the samples on porous carbon (ESI, Fig. 2†). Both systems show full reversibility after hydrogenation and dehydrogenation.

Hydrogen release properties

Fig. 6 shows the hydrogen release profiles of both $Mg_2Cu(H)$ prepared on porous carbon (a) and $Mg_2Cu(H)$ synthesized on non-porous carbon (b). As reference materials the following samples are also included: a sample containing a physical mixture of bulk $Mg_2Cu(H)$ with porous carbon (c) and MgH_2 in porous carbon made by melt infiltration (d).[25] The last reference was bulk $Mg_2Cu(H)$, which was prepared by induction melting (e).

Bulk $Mg_2Cu(H)$ (e) shows a broad H_2 desorption peak with a maximum around 415 °C. The peak temperature of the physical mixture of $Mg_2Cu(H)$ (c) was slightly decreased (410 °C) towards lower temperatures. MgH_2 molten on porous carbon showed a peak around 380 °C (d). The decrease in temperature for this composite is due to the presence of small MgH_2 particles inside the pores of the carbon support as we have described earlier.[25] The peak temperature of the $Mg_2Cu(H)$ composite on non-porous carbon (b) decreased further to approximately 340 °C. The most interesting desorption profile is from $Mg_2Cu(H)$ prepared on porous carbon (a), which shows the largest decrease in desorption temperature compared to the other samples. Compared to bulk $Mg_2Cu(H)$ (e), the desorption temperature is approximately 150 °C lower.

The benefits of using Cu are apparent from a comparison with the MgH_2 reference (Fig. 6(c)). The supported $Mg_2Cu(H)$–C composites release hydrogen at lower temperatures. The presence of the carbon support only has a minor effect on the

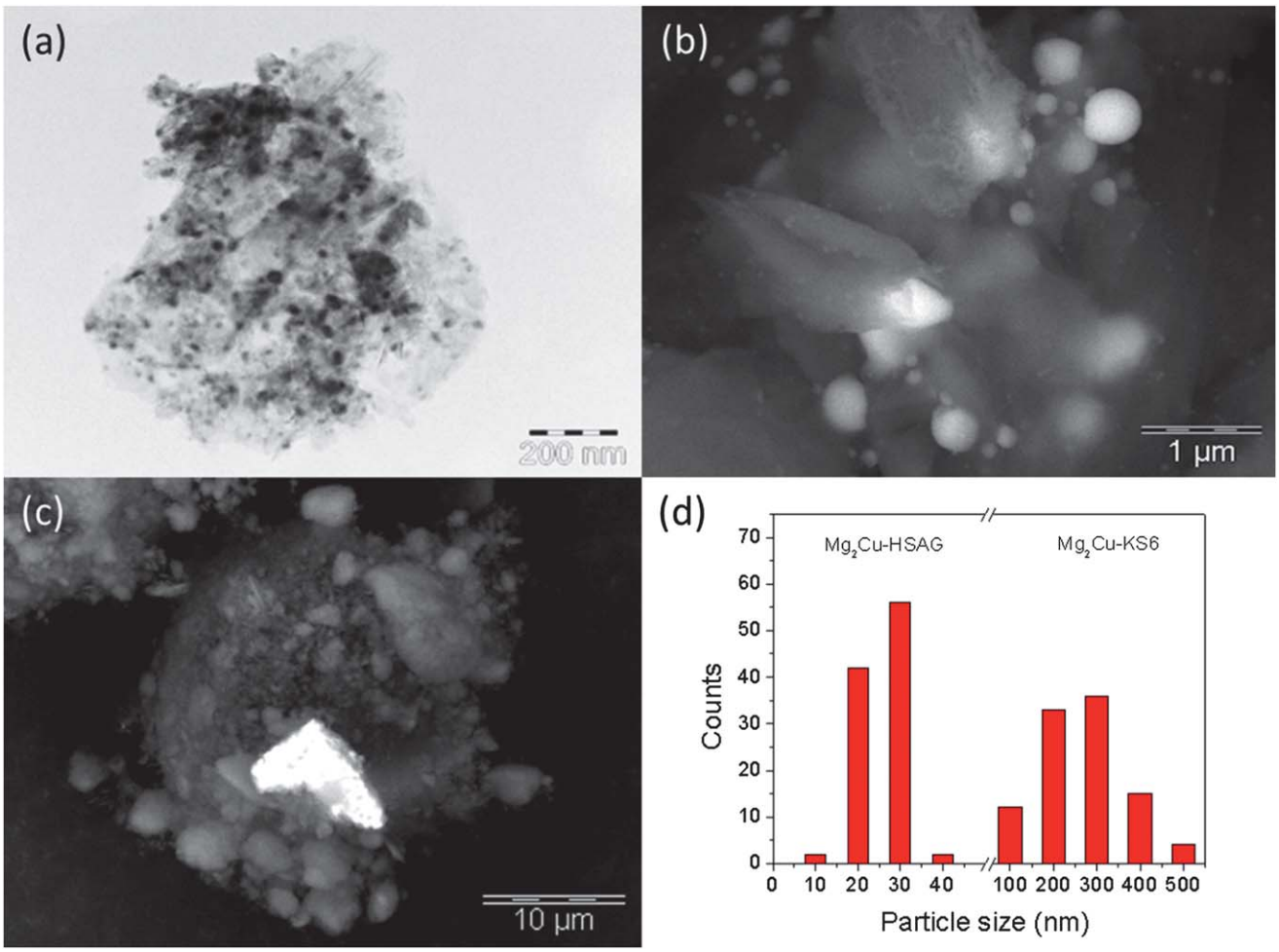

Fig. 5 Overview of electron microscope images. (a) Bright field TEM image of Mg_2Cu on porous carbon. (b) SEM image of Mg_2Cu on non-porous carbon from BSE. (c) SEM image from BSE of a physical mixture of powdered Mg_2Cu particles prepared by induction melting with porous carbon. In frame (d) the particle size distribution of Mg_2Cu on porous and non-porous carbon is shown as determined by the electron microscope images.

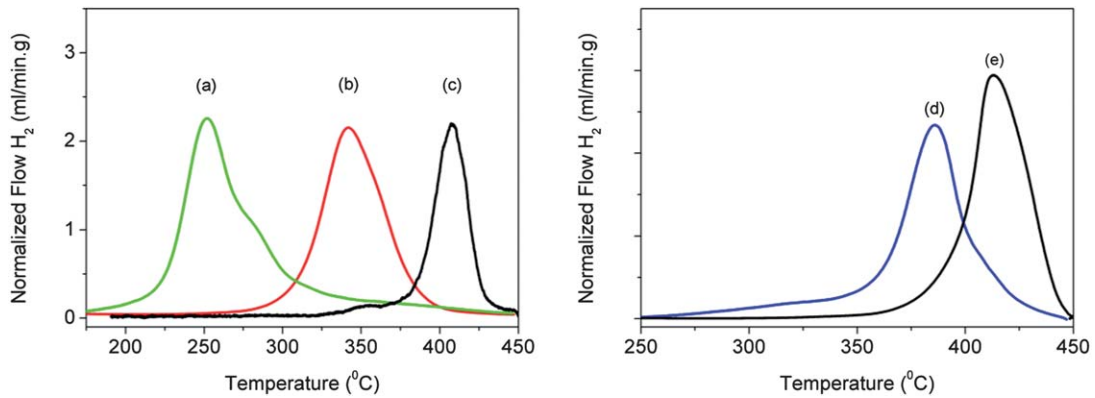

Fig. 6 TPD profiles (5 °C min^{-1}) of: (a) $Mg_2Cu(H)$ on porous carbon and (b) $Mg_2Cu(H)$ on non-porous carbon and (c) a physical mixture of $Mg_2Cu(H)$ bulk with porous carbon. The references are (d) MgH_2 on porous carbon and (e) bulk $Mg_2Cu(H)$.

temperature for hydrogen release when comparing the physical mixture (c) with pure $Mg_2Cu(H)$ (e). Structural characterization of these samples, as discussed in the previous section, revealed two major differences in the Mg_2Cu–C composites: particle size and distribution of the alloy on the support. By combining these results with the hydrogen release measurements, the trend is that smaller particles desorbed hydrogen at lower temperatures. Also, supported alloy particles on graphite showed lower temperatures for hydrogen release. The presence of a shoulder in sample (a) is most likely caused by the size distribution of the

sample, where particles with an average size of 20–30 nm were dominant as is shown in Fig. 5. This might also explain the broader peak of sample (b), where a larger difference in size distribution was found varying from 100 nm to 500 nm. The sieved bulk sample (c) turned out to be more uniform in size, leading to a narrower peak.

In summary, two effects are causing the shift in desorption temperature. The first is the effect of particle size, which causes the largest shift in the desorption temperature. The other effect is caused by the presence of graphite, which has a minor effect on the desorption reaction.

Cycling and the H_2 sorption equilibrium

Equilibrium desorption isotherms were measured volumetrically on Mg_2Cu–H on porous carbon (Fig. 7, left) after 2 initial sorption cycles. The isotherms show similar amounts of hydrogen being released at five different temperatures (250 °C, 275 °C, 300 °C, 325 °C and 350 °C). Only a single plateau was observed, which means that only one hydride phase is present. The equilibrium pressures were estimated from the center of the plateaus, which were at 0.75 wt% for the isotherms at 250 °C and 275 °C, and 1 wt% for the isotherms at 300 °C 325 °C and 350 °C. These plateau pressures were plotted in a van 't Hoff diagram (Fig. 7, right) and resulted in an enthalpy and entropy of the hydrogen desorption reaction of 66 (±3) kJ mol^{-1} H_2 and 126 (±10) J mol^{-1} K respectively. These values are comparable to earlier investigations.[12,21] The obtained enthalpy for this system is approximately 9 kJ mol^{-1} lower than MgH_2, which is causing the decrease in hydrogen release temperature for the $Mg_2Cu(H)$ system. Therefore, the hydrogen release properties of the Mg_2Cu on the porous carbon composite were kinetically and thermodynamically improved with respect to the MgH_2 system.

The reversibility of the hydrogen sorption reaction of $Mg_2Cu(H)$ on porous and non-porous carbon was measured gravimetrically (Fig. 8). Both samples were measured for 7 subsequent cycles and the onset temperature, where the weight loss starts occurring, is close to the thermodynamic equilibrium of ~250 °C at 1.3 bar H_2. $Mg_2Cu(H)$ on non-porous carbon (Fig. 8, left) shows an excellent reversibility close to the theoretical storage capacity of 2.6 wt%. For $Mg_2Cu(H)$ on porous carbon (Fig. 8: right), the first cycle showed almost the full storage capacity and the storage capacity decreased slightly for further cycling and stabilized at 2.0 wt%.

Comparing the slopes of the desorption profiles from $Mg_2Cu(H)$ both on porous carbon and non-porous carbon, the slope is steeper for $Mg_2Cu(H)$ on porous carbon. This indicates that the desorption kinetics are faster for this system, while there is no difference in the thermodynamics of both systems, since the onset temperature for desorption is the same. For instance, 80% of the total capacity was released after ~20 min at 280 °C for $Mg_2Cu(H)$ on porous carbon, while Mg_2Cu on non-porous carbon required ~60 min at a temperature of 320 °C. This is in line with the TPD results, where faster desorption kinetics were observed for $Mg_2Cu(H)$ on porous carbon due to a smaller average particle size.

It seems that Mg_2Cu on non-porous carbon with large crystallites has a better reversibility than Mg_2Cu on porous carbon containing smaller crystallites. This has also been observed by Jurczyk *et al.*[10] The reduction in hydrogen uptake was attributed to excess strain in the nanoparticles during hydrogen absorption and desorption or induced chemical disorder of the Mg–Cu lattice since Mg diffusion is required for the reaction $MgCu_2 \leftrightarrow Mg_2Cu$. On the other hand, it is also possible that the reduction in uptake could be due to oxidation of the active material due to impurities in the H_2-gas flow used in the experiments. Smaller particles tend to become oxidized faster and more material is lost due to the larger surface area to volume ratio of nanoparticles, assuming that only an oxide shell is formed.

Activation energy for hydrogen desorption of $Mg_2Cu(H)$–C

The lower reaction enthalpy for reaction (1) compared to pure MgH_2, 66 kJ mol^{-1} H_2 and 75 kJ mol^{-1} H_2 (ref. 30) respectively, results in a lower equilibrium temperature for the $Mg_2Cu(H)$ system.

However, TPD results have shown that there is still a large kinetic difference between the different $Mg_2Cu(H)$ phases

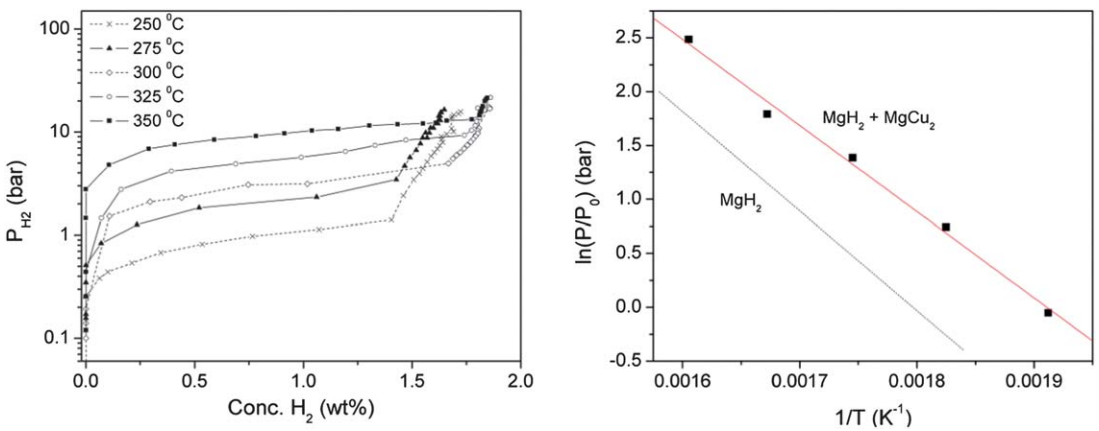

Fig. 7 Left: H_2 desorption isotherms of $Mg_2Cu(H)$ on porous carbon measured at 250 °C, 275 °C, 300 °C, 325 °C and 350 °C. Right: resulting van 't Hoff plot of $Mg_2Cu(H)$ on porous carbon. The dashed line stands for the reported phase equilibrium between Mg and MgH_2 with $\Delta H = 75$ kJ mol^{-1} H_2 and $\Delta S = 136$ J mol^{-1} K.[29]

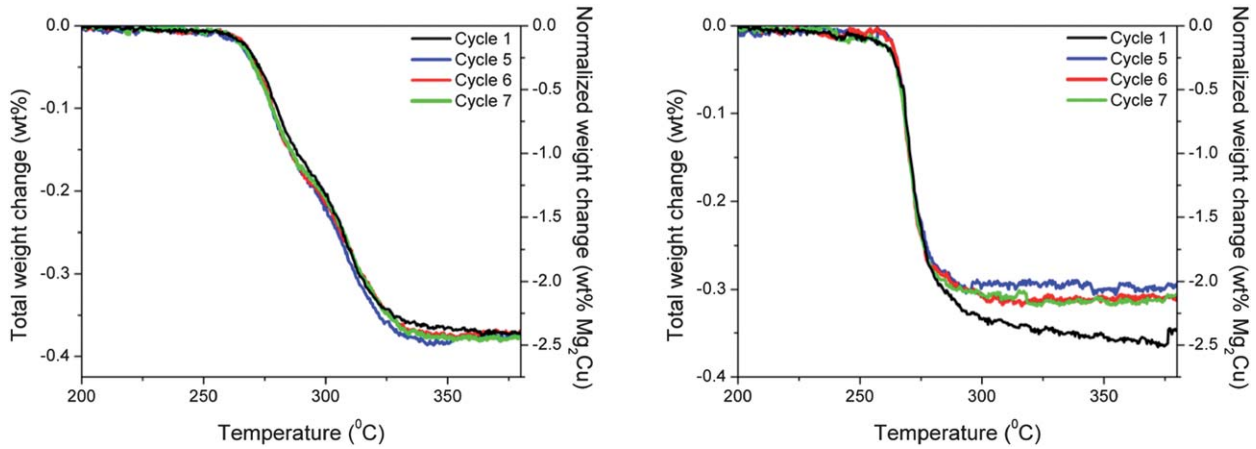

Fig. 8 H_2 desorption cycles measured gravimetrically of 15 wt% $Mg_2Cu(H)$ on carbon at 1.3 bar H_2 atmosphere with a heating ramp of 1 °C min^{-1}. The total and normalized weight change is shown. The quantity of hydrogen released is normalized to the total amount of $Mg_2Cu(H)$, which has a theoretical capacity of 2.6 wt% H_2. Left: $Mg_2Cu(H)$ on non-porous carbon. Right: $Mg_2Cu(H)$ on porous carbon.

supported on carbon. To study this difference, a Kissinger analysis was performed to obtain more information on the hydrogen release kinetics.[31]

An interesting trend of a decreasing activation energy (E_A) from the bulk (a) to $Mg_2Cu(H)$ on non-porous carbon (b) and $Mg_2Cu(H)$ on porous carbon (c) was observed (Table 2 and ESI, Fig. 3†). Bulk $Mg_2Cu(H)$ (d) resulted in similar values for the activation energy and pre-exponential factor as sample (c). Thus, the kinetic properties of $Mg_2Cu(H)$ did not change significantly by only adding carbon.

In Fig. 9, the activation energy is plotted against the Mg_2Cu particle sizes. Not only a decrease for the activation energy was found for smaller particles, but also the pre-exponential factor (A_0) is increasing for smaller particles. The value for the activation energy of the bulk reference is close to what has been found for the hydrogen desorption of pure MgH_2 (126 kJ mol^{-1}).[32]

The decrease in activation energy for the supported Mg_2Cu particles on porous carbon (a) and non-porous carbon (b) compared to the bulk reference (c) is quite remarkable. Earlier investigations have shown that the activation energy of the hydrogen sorption reaction of pure MgH_2 did not change for different particle- and grain sizes.[33] On the other hand, reaction (1) requires the diffusion of Mg atoms to obtain Mg_2Cu. Lei *et al.* have proposed a model on how this might occur.[11] This mechanism involves formation of new crystal boundaries of $Mg(H_2)$, $MgCu_2$ and Mg_2Cu during the hydrogen sorption reaction. Smaller particles might have a lower activation energy for reaction (1), because the diffusion distance for Mg atoms to reform Mg_2Cu is shorter. This also might explain the increasing pre-exponential factor. The larger grain boundary between the MgH_2 and $MgCu_2$ phases provides a higher statistical probability for the solid-state reaction of $MgCu_2 \leftrightarrow Mg_2Cu$ to occur, which favors decomposition of MgH_2. The movement of the phase boundary between MgH_2 and $MgCu_2$ is most likely the rate-limiting step, since solid-state diffusion of atoms requires thermal activation.

Another aspect is the effect of the used carbon supports. With our synthesis method, the alloy particles are brought in close contact with the carbon support. This could have an influence on the electronic structure of the alloy leading to a lower activation energy. A similar trend was observed for MgH_2–C nanocomposites.[34] Smaller and well dispersed alloy particles

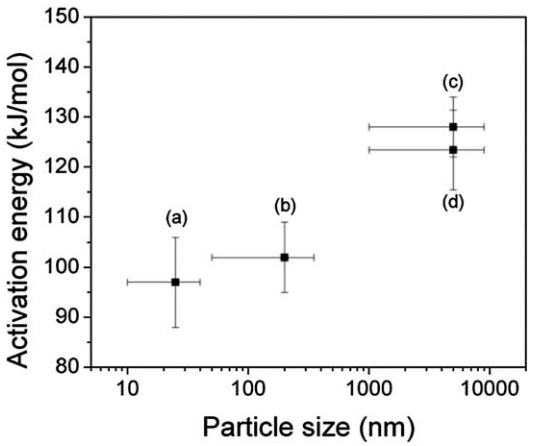

Fig. 9 Relationship between particle size and activation energy for hydrogen desorption of: (a) $Mg_2Cu(H)$ on porous carbon. (b) $Mg_2Cu(H)$ on non-porous carbon. (c) Bulk physical mixture of $Mg_2Cu(H)$ with porous carbon. (d) Bulk Mg_2Cu without carbon.

Table 2 Calculated values for the activation energy (E_A) and pre-exponential factor (A_0). The maximum peak temperatures are given for a heating rate of 5 °C min^{-1} (Fig. 6)

Sample	T_{max} (°C)	E_A (kJ mol^{-1})	A_0 (s^{-1})
(a) $Mg_2Cu(H)$, (~20 nm)	251	97, (±9)	1.1×10^7, ($\pm 0.1 \times 10^7$)
(b) $Mg_2Cu(H)$, (~300 nm)	341	102, (±7)	1.0×10^6, ($\pm 0.1 \times 10^6$)
(c) $Mg_2Cu(H)$, (>1 μm)	407	128, (±6)	4.7×10^4, ($\pm 0.2 \times 10^4$)
(d) $Mg_2Cu(H)$, (>1 μm)	406	123, (±8)	4.9×10^4, ($\pm 0.2 \times 10^4$)

have relatively more contact with the support material, which enhances the effect. In this case sample (a) has the best dispersion and consists of the smallest crystallites, thus has the lowest activation energy.

Conclusions

We have successfully applied a new method to obtain Mg_2Cu alloy nanoparticles supported on carbon. There are clear synergetic effects of nanosizing and using a carbon support. Different sizes of Mg_2Cu were obtained, where the average size of Mg_2Cu nanoparticles was 20 nm on a porous carbon support. The activation energy for hydrogen desorption of these nanoparticles was lowered from 128 ($\pm$6) for a physical mixture of bulk Mg_2Cu with porous carbon to 97 ($\pm$9) kJ mol^{-1} for supported Mg_2Cu nanoparticles on porous carbon. We were able to improve the kinetics for the solid-state reaction involved in this material. This new synthesis method to obtain nanomaterials with enhanced kinetic properties could be relevant to the development of other Mg-based alloy nanomaterials for applications in hydrogen storage or batteries in the future.

Acknowledgements

This work was financially supported by a grant from the Dutch organization for scientific research (NWO Vidi (016.072.316)) and is part of the NWO 'van Gogh' program. Part of this work was supported by the COST Action MP1103 "Nanostructured materials for solid-state hydrogen storage". M. Versluijs-Helder and J. D. Meeldijk are greatly acknowledged for obtaining the SEM and TEM images. A. M. J. van der Eerden is acknowledged for his technical support and we would like to thank our colleague G. J. Kastelein from the Faculty of Geosciences for lending his high-pressure equipment for the experiments. We are grateful to Timcal for providing us the carbon samples.

Notes and references

1 B. Sakintuna, F. Lamari-Darkrim and M. Hirscher, *Int. J. Hydrogen Energy*, 2007, **32**, 1121–1140.
2 I. P. Jain, C. Lal and A. Jain, *Int. J. Hydrogen Energy*, 2010, **35**, 5133–5144.
3 G. Liang, J. Huot, S. Boily, A. Van Neste and R. Schulz, *J. Alloys Compd.*, 1999, **292**, 247–252.
4 N. Hanada, T. Ichikawa, S. Hino and H. Fujii, *J. Alloys Compd.*, 2006, **420**, 46–49.
5 J. L. Murray, *Bull. Alloy Phase Diagrams*, 1982, **3**, 60–74.
6 A. A. Nayeb-Hashemi and J. B. Clark, *Bull. Alloy Phase Diagrams*, 1985, **6**, 238–244.
7 D. Moser, D. J. Bull, T. Sato, D. Noréus, D. Kyoi, T. Sakai, N. Kitamura, H. Yusa, T. Taniguchi, W. P. Kalisvaart and P. Notten, *J. Mater. Chem.*, 2009, **19**, 8150–8161.
8 C. Milanese, A. Girella, G. Bruni, V. Berbenni, P. Cofrancesco, A. Marini, M. Villa and P. Matteazzi, *J. Alloys Compd.*, 2008, **465**, 396–405.
9 A. Andreasen, M. B. Sørensen, R. Burkarl, B. Møller, A. M. Molenbroek, A. S. Pedersen, T. Vegge and T. R. Jensen, *Appl. Phys. A: Mater. Sci. Process.*, 2006, **82**, 515–521.
10 M. Jurczyk, I. Okonska, W. Iwasieczko, E. Jankowska and H. Drulis, *J. Alloys Compd.*, 2007, **429**, 316–320.
11 J. P. Lei, H. Huang, X. L. Dong, J. P. Sun, B. Lu, M. K. Lei, Q. Wang, C. Dong and G. Z. Cao, *Int. J. Hydrogen Energy*, 2009, **34**, 8127–8134.
12 H. Shao, Y. Wang, H. Xu and X. Li, *J. Solid State Chem.*, 2005, **178**, 2211–2217.
13 M. X. Tanaka, N. Takeichi, H. T. Takeshita and T. Kiyobayashi, *Mater. Trans.*, 2008, **49**, 2698–2701.
14 F. Cuevas, D. Korablov and M. Latroche, *Phys. Chem. Chem. Phys.*, 2012, **14**, 1200–1211.
15 P. Cao, L. Lu and M. O. Lai, *Mater. Res. Bull.*, 2001, **36**, 981–988.
16 S. D. Beattie, U. Setthanan and G. S. McGrady, *Int. J. Hydrogen Energy*, 2011, **36**, 6014–6021.
17 T. K. Nielsen, F. Besenbacher and T. R. Jensen, *Nanoscale*, 2011, **3**, 2086–2098.
18 P. E. De Jongh and P. Adelhelm, *ChemSusChem*, 2010, **3**, 1332–1348.
19 C. Zlotea, F. Cuevas, J. Andrieux, C. Matei Ghimbeu, E. Leroy, E. Léonel, S. Sengmany, C. Vix-Guterl, R. Gadiou, T. Martens and M. Latroche, *Nano Energy*, 2013, **2**, 12–20.
20 R. Bogerd, P. Adelhelm, J. H. Meeldijk, K. P. De Jong and P. E. De Jongh, *Nanotechnology*, 2009, **20**, 204019.
21 J. J. Reilly and R. H. Wiswall, *Inorg. Chem.*, 1967, **6**, 2220–2223.
22 A. A. Nayeb-Hashemi and J. B. Clark, *Bull. Alloy Phase Diagrams*, 1984, **5**, 36–43.
23 T. Toupance, M. Kermarec and C. Louis, *J. Phys. Chem. B*, 2000, **104**, 965–972.
24 A. R. Silva, J. L. Figueiredo, C. Freire and B. De Castro, *Catal. Today*, 2005, **102–103**, 154–159.
25 P. E. De Jongh, R. W. P. Wagemans, T. M. Eggenhuisen, B. S. Dauvillier, P. B. Radstake, J. D. Meeldijk, J. W. Geus and K. P. De Jong, *Chem. Mater.*, 2007, **19**, 6052–6057.
26 B. A. Hunter, *IUCR Powder Diffraction*, 1997, vol. 22, p. 21.
27 F. Gingl, P. Selvam and L. Yvon, *Acta Crystallogr., Sect. B: Struct. Sci.*, 1993, **49**, 201.
28 T. Ohba, Y. Kitano and Y. Komura, *Acta Crystallogr., Sect. B: Struct. Sci.*, 1984, **40**, 1.
29 A. Karty, J. Grunzweig-Genossar and P. S. Rudman, *J. Appl. Phys.*, 1979, **50**, 7200–7209.
30 P. Larsson, C. M. Araújo, J. A. Larsson, P. Jena and R. Ahuja, *Proc. Natl. Acad. Sci. U. S. A.*, 2008, **105**, 8227–8231.
31 H. E. Kissinger, *Anal. Chem.*, 1957, **29**, 1702–1706.
32 C. M. Stander, *J. Inorg. Nucl. Chem.*, 1977, **39**, 221–223.
33 D. Fátay, Á. Révész and T. Spassov, *J. Alloys Compd.*, 2005, **399**, 237–241.
34 Z. Zhao-Karger, J. Hu, A. Roth, D. Wang, C. Kübel, W. Lohstroh and M. Fichtner, *Chem. Commun.*, 2010, **46**, 8353–8355.